Mitochondrially targeted deferasirox kills cancer cells *via* simultaneous iron deprivation and ferroptosis induction.

Sukanya B Jadhav[1,2*], Cristian Sandoval-Acuña[1*], Yaiza Pacior[1,2], Kristyna Klanicova[1,2], Kristyna Blazkova[1], Radislav Sedlacek[3], Jan Stursa[1], Lukas Werner[1] and Jaroslav Truksa[1,#]

[1] Institute of Biotechnology of the Czech Academy of Sciences, BIOCEV Research Center, Vestec, Czech Republic

[2] Faculty of Science, Charles University, Prague, Czech Republic

[3] Czech Centre for Phenogenomics, Institute of Molecular Genetics of the Czech Academy of Sciences, Vestec, Czech Republic

* Shared first authors

[#] Corresponding author: Jaroslav Truksa, Prumyslova 595, Vestec 252 50, Czech Republic, +(420) 325 873 735 jaroslav.truksa@ibt.cas.cz

Conflict-of-interest statement

J.T., C.S.A., L.W., J.S., and K.B. acknowledge the patent application "3,5-bis(phenyl)-1h-heteroaryl derivatives as medicaments" with Smartbrain s.r.o. The authors declare that they have no conflict of interest.

Abstract

Iron chelation has been proposed as an anti-cancer approach; however, iron chelators are generally non-specific for cancer cells and rely on the higher sensitivity of malignant cells to iron deprivation and accumulation of the drug in tumor tissue *via* the enhanced permeability and retention effect. Here, we present mitochondrially targeted deferasirox (mitoDFX), a redox-active iron chelator that deprives cells of biologically active iron, as evidenced by a decrease in [Fe-S] cluster and heme-containing proteins. Notably, mitoDFX also depletes the major cellular antioxidant glutathione and induces lipid peroxidation, both of which are hallmarks of ferroptosis, resulting in selective induction of cell death in cancer cells. In summary, targeting deferasirox into the mitochondria results in an agent that has a unique ability to elicit iron deprivation and produce toxic lipid peroxides *via* its redox activity, thus harnessing the dual nature of iron in a single molecule to combat cancer.

Introduction

Iron is a critical trace element that participates in many biological processes including oxygen transport, metabolism, cell cycle progression, and DNA synthesis and repair (1-6). Furthermore, iron is a key component of the enzyme cofactors heme and iron-sulfur [Fe-S] clusters, which are partially synthesized in mitochondria, making them central organelles of cellular iron metabolism (4, 7-9).

Although iron is essential for the normal physiological functions of cells, excess iron leads to the generation of reactive oxygen species (ROS) *via* the Fenton and Haber-Weiss reaction (9, 10). The hydroxyl radical generated during this process is one of the most toxic oxidants that damage biomolecules, including lipids, leading to a specific form of cell death termed "ferroptosis" (11).

Cancers are usually characterized by excessive proliferation and altered metabolic needs including high iron demand (12, 13). Studies have demonstrated abnormal iron homeostasis in cancers, coupled with increased uptake and utilization and decreased efflux of iron, defining a signature that is correlated with poor clinical outcomes (10, 14, 15). As tumor cells are highly dependent on iron for growth and proliferation, they are more sensitive to iron depletion than normal cells. Therefore, targeting iron metabolism is considered a therapeutic strategy for cancer treatment. Iron chelators are small molecules that contain oxygen, nitrogen, or sulfur donor atoms that form high-affinity coordinate bonds with iron. Several studies have demonstrated the role of iron chelators as potential anti-tumor agents (12, 16-19). There are two classes of iron chelators: redox-active and redox-inactive. Commercially available iron chelators, including deferiprone (DFP), deferasirox (DFX), and desferrioxamine (DFO), are commonly used in clinical settings (20, 21). Iron can form up to six bonds that are all occupied in the complex with the hexadentate chelator DFO, rendering it inert and preventing its use in cellular processes (22). DFO was the first iron chelator tested for cancer treatment; however, it has poor bioavailability and a very short lifespan (21). In contrast, deferasirox is a tridentate redox-active iron chelator that is orally available and has a longer half-life in plasma (20). DFX showed anti-proliferative

3

effects on experimental breast (23), lung (17), pancreatic (24), gastric cancers (25), and myeloid leukemia (26) by inhibiting DNA replication, inducing DNA fragmentation, and blocking cells in the G0-G1 phase of the cell cycle. However, the chelators described so far are not targeted to cancer cells and rely on the higher sensitivity of cancer cells to iron deprivation, defective tumor vasculature, and the EPR effect.

Recently, mitochondrial targeting of anti-cancer compounds *via* delocalized lipophilic triphenylphosphonium cations has proven to be an effective and more specific strategy to deliver experimental anti-cancer drugs (27-30). Since cancer cells have a higher mitochondrial membrane potential, which drives the preferential accumulation of TPP^+ in the mitochondria, it selectively targets malignant cells while sparing non-malignant cells (31, 32). Furthermore, mitochondrially targeted iron chelators based on mitochondria-homing SS-like peptides have been synthesized and tested as antioxidants against UV damage and possible probes for measuring mitochondrial iron, although they have not been proposed as anti-tumor agents (33, 34).

Here, we report the synthesis of mitochondrially targeted deferasirox (mitoDFX) and demonstrate that it potently induces cell death in cancer cells at nanomolar concentrations by employing the dual nature of iron to synergistically combat cancer, as it not only deprives cells of biologically active iron but also depletes the major cellular antioxidant glutathione and induces lipid peroxidation.

Results

MitoDFX exhibits anti-proliferative and cytotoxic effects against breast cancer cells in vitro

Deferasirox is a redox-active iron chelator that inhibits the growth of several types of cancer cells *in vitro* and *in vivo* (17, 24, 26). To deliver the iron chelator DFX into mitochondria, the central organelle of iron metabolism, we synthesized its mitochondrially targeted analog by tagging the chelator with a triphenylphosphonium (TPP^+) moiety via a linker, which we refer to as mitochondrially targeted

deferasirox (mitoDFX) **(Fig. 1A)**. In this study, we tested whether targeting DFX to the mitochondria enhanced its anti-cancer properties and increased its selectivity for cancer cells.

To examine the anti-proliferative activity of mitoDFX and compare it with that of the parental agent, we treated a panel of cancer cell lines of breast, melanoma, lung, pancreatic, and ovarian origin, together with normal fibroblasts. Our results demonstrated that mitoDFX decreased the number of viable cancer cells at markedly lower concentrations than DFX **(Fig. 1B and S1A)**, with IC_{50} values in the nM range, thus enhancing the effect by almost three orders of magnitude **(Table S1)**. To further understand the inhibitory effect of mitoDFX, we performed real-time monitoring of cell proliferation and death induction using a Lumascope S720 microscope. The results demonstrated a cytostatic effect on breast cancer cells at nanomolar concentrations **(Fig. 1C and S1B)**. Importantly, a cytotoxic effect was detected only in malignant MCF7 cells exposed to mitoDFX, and not in BJ fibroblasts even at 1 µM **(Fig. 1D)**, demonstrating the selectivity of the cytotoxic effect of mitoDFX against cancer cells (see also **Table S1**). In contrast, treatment with 10 µM DFX showed only low cytostatic and cytotoxic activities **(Fig. 1E, F, and S1C)**. Next, annexin V/PI staining was performed to confirm the cytotoxic effect of the compounds. Our results showed an enhanced cytotoxic effect after 48 h of treatment with 1 µM mitoDFX in both MCF7 and MDA-MB-231 malignant breast cancer cells while sparing BJ cells **(Fig. 1G and S1D)**. Interestingly, 10 µM DFX did not elicit a significant cytotoxic effect in contrast to mitoDFX **(Fig. 1H and S1E)**. Moreover, 30 nM mitoDFX treatment for 72h arrested proliferation at the G_1 phase of the cell cycle in MCF7 and MDA-MB-231 breast cancer cells but not in BJ fibroblasts **(Fig. 1I and S1F)**. Notably, a similar effect was not observed in cancer cells even at markedly higher concentrations of DFX (10 µM) **(Fig. 1I and S1F)**. Taken together, these results illustrate the significant cytostatic and cytotoxic effects of nanomolar concentrations of mitoDFX against cancer cells, while sparing non-malignant cells. Additionally, DFX was unable to elicit a similar response unless used at concentrations higher than 10 µM, at which point it did not discriminate between malignant and non-malignant cells.

MitoDFX causes destabilization of iron metabolism in breast cancer cells

Given that mitoDFX is an iron chelator, we first explored whether it alters the level of intracellular Fe^{2+} in breast cancer cells (MCF7 and MDA-MB-231) and BJ fibroblasts. Confocal microscopy results demonstrated a significant decrease in the fluorescence intensity of the FerroOrange dye in breast cancer cells after treatment with mitoDFX for 24 h, suggesting that mitoDFX reduced the level of free intracellular Fe^{2+} **(Fig. 2A, B, and S2A, B)**, whereas no change was observed in BJ cells **(Fig. 2C, D)**. Next, we treated the cells with mitoDFX at a low dose of 50 nM for 60 h and did not detect any change in Fe^{2+} level, demonstrating that low concentrations of mitoDFX did not alter the total intracellular iron pool **(Fig. 2A, B, C, D and S2A, B)**. This could be a result of the specific targeting of DFX into the mitochondria or of compensatory mechanisms activated by cells in response to low-dose chelation.

We then evaluated the effects of mitoDFX on cellular iron metabolism markers. The level of the iron-uptake protein TFRC was significantly upregulated after 60 h of treatment with 50 nM mitoDFX in MCF7 and MDA-MB-231 cells, but not in BJ cells, whereas the level of DMT1 was increased in all cell lines. Ferritin (FTH) levels were decreased in MCF7 and MDA-MB-231 cells, with no change in BJ cells. Finally, the iron exporter ferroportin (FPN) was decreased only in MCF7 cells, and the iron sensor FBXL5 was not altered in any of the cell lines **(Fig. 2E and S2C).** A similar pattern was observed after 24 h of exposure to 1 µM mitoDFX, although ferritin levels were increased in MCF7 cells **(Fig. 2F and S2D)**.

To further investigate the effect of mitoDFX on mitochondrial iron, we evaluated its level using the MitoFerroGreen probe. Confocal microscopy results demonstrated a considerable decrease in the level of mitochondrial Fe^{+2} in both malignant cells after short- and long-term mitoDFX treatment **(Fig. 3A, B and S2E, F)**. In contrast, mitoDFX treatment of BJ cells decreased mitochondrial Fe^{2+} level only mildly after 24 h and showed no significant change after 60 h of exposure **(Fig. 3C, D)**. Overall, our data illustrates that mitoDFX specifically reduces the level of mitochondrial Fe^{2+} in cancer cells, thereby confirming its effects on mitochondria and selectivity against malignant cells.

6

As iron is utilized in the mitochondria to form either [Fe-S] clusters or heme, we evaluated the levels of proteins containing either cofactor using western blotting. Our results showed that mitoDFX impaired [Fe-S] cluster assembly and heme synthesis, as the levels of iron-containing proteins that participate in the ETC, such as NDUFA9, SDHB, UQCRFS1, and mtCO1, were strongly reduced upon long-term exposure to 50 nM mitoDFX in malignant cells, with no significant changes observed in BJ fibroblasts **(Fig. 3E and S2G)**. Similar changes were also observed after 24 h of incubation with 1 µM mitoDFX, with a dramatic decrease in breast cancer cells and only a slight decrease in NDUFA9 and UQCRFS1 in BJ cells **(Fig. 3F and S2H)**. We further studied the mitochondrial enzymes responsible for the biosynthesis of [Fe-S] clusters (ISCU) and heme (FECH). After treatment with 50 nM mitoDFX for 60 h, we detected a significant decrease in both proteins in malignant cells, with only slight or no change observed in BJ fibroblasts **(Fig. 3E and S2G)**. Similarly, exposure to 1 µM mitoDFX for 24 h led to diminished levels of both ISCU and FECH in malignant breast cancer cells, whereas these levels were increased in BJ cells **(Fig. 3F and S2H)**. Additionally, we evaluated the expression of proteins of the cytosolic iron-sulfur assembly pathway (CIAO1, MMS19, and NUBP1) and found that these proteins did not change or even moderately increased in all three cell lines tested **(Fig. S2I, J)**.

Overall, these results demonstrate that mitoDFX deprives cells of the available mitochondrial pool of iron and reduces the levels of mitochondrial [Fe-S] cluster- and heme-containing proteins. Notably, the cytosolic [Fe-S] cluster assembly machinery remained intact indicating a specific effect on mitochondria.

MitoDFX alters mitochondrial proteome and reduces mitochondrially coded transcripts

To gain a more comprehensive overview of the effects of mitoDFX on both cellular and mitochondrial proteomes, we performed proteomic analysis using mass spectrometry. The results showed a completely different pattern of proteins affected by mitoDFX and DFX treatment **(Fig. 4A, B)**. Treatment with 50 nM mitoDFX downregulated the expression of proteins involved in mitochondrial translation,

7

biogenesis, respiration, and antioxidant defense **(Fig. 4A)**. Notably, treatment with 50 nM mitoDFX dramatically depleted the components of all mitochondrial respiratory complexes; however, these changes could not be recapitulated with 10 μM DFX **(Fig. S3A, B, C)**. Additionally, our results showed that mitoDFX exposure for 24 and 60 h reduced the protein subunits involved in both general and mitochondrial transcription and replication. Furthermore, we detected a dramatic reduction in the subunits of mitochondrial ribosomes and several tRNA ligases involved in mitochondrial translation while these changes were mild or absent after DFX treatment **(Fig. S3D, E)**. The effect on mitochondrial transcription was confirmed by the markedly reduced levels of mitochondrial transcripts **(Fig. S3F)**. Detailed analysis of the affected pathways was performed using the Reactome pathway knowledgebase(35) and is provided in **Supplementary File 1**.

MitoDFX inhibits the tricarboxylic acid cycle (TCA) cycle

Since respiration and the TCA cycle were among the most deregulated pathways identified by the Reactome analysis, we next assessed the effect of mitoDFX on the relative levels of glycolysis and TCA cycle intermediates. We found that the levels of glycolysis products significantly decreased after mitoDFX treatment, in line with the trend of reduced fructose-1,6-bisphosphate in mitoDFX-treated cells. Similarly, the metabolic intermediates of the TCA cycle, such as citric acid, isocitric acid, succinyl-CoA, fumarate, and malate, were drastically reduced in the mitoDFX-treated samples. In contrast, acetyl-CoA, α-ketoglutarate, and succinate were the only derivatives that remained unchanged after mitoDFX treatment **(Fig. S4)**. These findings suggest that the TCA cycle no longer runs as a canonical cycle and cannot support associated metabolic pathways, such as lipogenesis, urea cycle, or amino acid metabolism, hampering cell proliferation.

8

MitoDFX causes a reduction in mitochondrial respiratory activity and decreases the amount and assembly of mitochondrial respiratory supercomplexes

Oxidative phosphorylation involves series of metabolic reactions that occur within mitochondria to produce ATP. As we previously observed significantly decreased levels of several [Fe-S]- and heme-containing subunits of the ETC, we next examined the effect of mitoDFX on ETC-dependent oxygen consumption. Our results showed that mitoDFX inhibited mitochondrial respiration at a concentration of 1 μM in both malignant cell lines, with only a minor impact on BJ cells. Basal respiration, ATP production, and maximal respiration were reduced in breast cancer cells after 1 h of mitoDFX treatment **(Fig. S5A)**. We further showed that a significantly higher dose of DFX was required to impair the ETC compared to mitoDFX **(Fig. S5B)**.

Since mitoDFX reduced oxygen consumption, we assessed the amount and assembly of respiratory supercomplexes using blue native electrophoresis (BNE). A significant decrease in the levels of CI, CII, CIII, and CIV was observed in MCF7 breast cancer cells after treatment with 100 nM mitoDFX for 24 h, whereas such changes were not observed in non-malignant BJ fibroblasts, where they became apparent only at a concentration of 1 μM **(Fig. 5A)**. A reduction in complexes I, III, and IV was also observed in MDA-MB-231 breast cancer cells **(Fig. S5C)**.

To assess the functional significance of this finding, we measured intracellular ATP levels in breast cancer cells and BJ fibroblasts treated with varying concentrations of mitoDFX in the presence or absence of either 50 mM 2-deoxyglucose (2-DG) or 2 μM oligomycin. Treatment with mitoDFX and 2-DG induced a significant ATP depletion in MCF7 and MDA-MB-231 cells compared with BJ cells. In contrast, treatment with mitoDFX alone or in combination with oligomycin did not cause any changes in ATP levels in any of the cell lines tested, suggesting that the cells were able to replenish the ATP pool *via* glycolysis to compensate for the loss of mitochondrial respiration **(Fig. S5D)**.

MitoDFX induces a decrease in mitochondrial membrane potential and induces mitochondrial fragmentation and redistribution

Mitochondria are dynamic organelles that continuously undergo fission and fusion. Fusion is connected with thin and elongated mitochondria; however, stress conditions induce mitochondrial fission, resulting in small and fragmented mitochondria(36). Our confocal microscopy results demonstrated that treatment of MCF7-mitoGFP expressing cells with mitoDFX led to a significant increase in the number of mitochondria and a decrease in the mean mitochondrial volume **(Fig. 5B, C, D)**, indicating the induction of mitochondrial fragmentation and redistribution. Furthermore, a shift of mitochondria from the perinuclear compartment towards the radial regions of the cell was observed upon mitoDFX treatment **(Fig. 5E)**.

As mitochondrially targeted drugs that comprise the TPP$^+$ moiety are known to disrupt membrane potential and mitochondrial functionality (27, 29, 30), we next examined the status of mitochondrial membrane potential (MMP) using the tetramethylrhodamine (TMRM) probe. Treatment with 50 nM mitoDFX for 60 h significantly reduced MMP in all tested cells **(Fig. S6A)**, yet 24 h treatment with mitoDFX reduced mitochondrial TMRM accumulation only in MCF7 and MDA-MB-231 cells, whereas no change was observed in BJ cells **(Fig. S6B)**.

Dysfunctional low-membrane-potential mitochondria are often degraded in lysosomes by mitophagy. Therefore, we examined whether this degradative process was induced by mitoDFX using the Mtphagy Dye, which stains acidified mitochondria, and documented enhanced mitophagy upon treatment with mitoDFX in malignant cells **(Fig.S6C)**.

Overall, these results demonstrate that mitoDFX causes mitochondrial dysfunction that involves the loss of membrane potential, disassembly of respiratory complexes, induction of mitochondrial fission, and markedly increased mitophagy in malignant breast cancer cells, but not in non-malignant cells.

MitoDFX increases ROS levels and induces lipid peroxidation

Mitochondria are an important source of reactive oxygen species (ROS). Mitochondrial dysfunction and depolarization result in increased ROS production, which in turn causes more damage to the organelles. Considering that mitoDFX is, in principle, a redox-active iron chelator, we evaluated whether mitoDFX triggered oxidative stress by evaluating mitochondrial and cellular ROS levels. A 60 h treatment with 50 nM mitoDFX significantly induced mitochondrial superoxide levels in MDA-MB-231 cells, with the same trend observed in MCF7 cells **(Fig. 5F and S7A)**. Cellular ROS levels were significantly increased in MCF7 cells, and a similar trend was observed in MDA-MB-231 cells **(Fig. 5G and S7B)**. Importantly, mitochondrial and cellular ROS levels did not increase in BJ cells after long-term treatment with mitoDFX **(Fig. 5F, G)**, confirming the selectivity of this agent. In contrast, mitochondrial and cellular ROS levels were elevated in all cell lines after treatment with higher concentrations (1 and 5 µM) for 24 h **(Fig. S7C, D)**. As high levels of ROS damage biomolecules including lipids (37), we assessed mitochondrial lipid peroxidation using the MitoPeDPP fluorescent probe (38) and found it to be significantly higher in MCF7 and MDA-MB-231 breast cancer cells 60 h after treatment compared to BJ fibroblast cells **(Fig. 6A and S7E)**. Similar results were obtained after 1 h of mitoDFX treatment in breast cancer cells with a higher dose of 1 µM, and BJ fibroblasts were also affected in this case **(Fig. S7F)**, yet it is important to note that at 1 µM, mitoDFX killed cancer cells only but not non-malignant BJ cells **(Fig. 1D and S1B)**.

MitoDFX induces oxidative stress via exhaustion of reduced glutathione

Cellular protection against oxidative stress is primarily mediated by glutathione (GSH), an active tripeptide comprising glutamic acid, glycine, and cysteine. Therefore, we assessed GSH levels using the GSH/GSSG-Glo™ assay and found that GSH levels were significantly reduced after 60 h of exposure to 50 nM mitoDFX in MCF7 and MDA-MB-231 cells, but not in BJ cells **(Fig. 6B and S7G)**. Since the redox balance within the cell is determined by the ratio of reduced/oxidized glutathione (GSH/GSSG ratio), we

11

also evaluated the total glutathione levels (GSH + 2 × GSSG) and observed their reduction only in MCF7 cells treated long-term with mitoDFX **(Fig. S7H)**, whereas a slight reduction was observed in MDA-MB-231 and BJ cells. We also observed a decrease in the GSH/GSSG ratio after long-term mitoDFX treatment of MCF7 cells **(Fig. S7I)**. Interestingly, no significant changes were observed in MDA-MB-231 and BJ cells after mitoDFX treatment for 24-60 h. This suggests that the shift in the GSH/GSSG ratio might be a critical factor leading to cell death, as MCF7 cells have IC_{50} values below 50 nM **(Fig. 1C, D)** and showed signs of oxidative damage. In contrast, MDA-MB-231 and BJ cells have IC_{50} values above 50 nM and showed signs of either a cytostatic effect (MDA-MB-231) or no effect (BJ) **(Fig. 1C, D, and S1B)**.

MitoDFX increases the NAD^+/NADH ratio and synergizes with a pentose phosphate pathway inhibitor

Given the vital role of reducing equivalents such as NAD^+/NADH and $NADP^+$/NADPH in regulating cellular redox status, glutathione metabolism, and mitochondrial function, we evaluated the redox status of these redox couples. Our results showed that the NAD^+/NADH ratio was significantly increased in MCF7 cells after 60 h and in MDA-MB-231 breast cancer cells after 24 h of exposure to 50 nM mitoDFX, whereas it remained unchanged in BJ cells **(Fig. S8A)**. The NAD^+/NADH ratio was altered by a decrease in NADH, suggesting that it was consumed. However, the $NADP^+$/NADPH ratio did not change after mitoDFX treatment in any of the tested cell lines **(Fig. S8B)**. It is well documented that cancer cells have an elevated pentose phosphate pathway (PPP) that generates NADPH to counteract high levels of ROS by allowing the continuous reduction of oxidized glutathione (39). Based on this fact and our finding that mitoDFX treatment did not alter the $NADP^+$/NADPH ratio, we used 6-aminonicotinamide (6-AN), an inhibitor of PPP, to assess whether this pathway may provide protection against mitoDFX. Interestingly, 6-AN markedly enhanced the cytotoxic effect of mitoDFX in MCF7 cells compared with mitoDFX treatment alone, confirming that the PPP pathway is actively utilized to protect cells from oxidative damage **(Fig. S8C)**.

Depletion of glutathione and loss of GPX4 sensitizes cells to mitoDFX-induced death

To confirm the importance of reduced glutathione in the effect of mitoDFX, we used buthionine sulfoximine (BSO), a potent inhibitor of γ-glutamylcysteine synthetase (γ-GCS) (40). Co-treatment of MCF7 cells with BSO and mitoDFX showed that BSO enhanced the cytostatic and cytotoxic effects of mitoDFX in MCF7 cells **(Fig. 6C)**. Similarly, sulfasalazine (SSZ), an inhibitor of the xCT-cystine/glutamate antiporter, demonstrated a stronger cytostatic effect in MCF7 cells in combination with mitoDFX **(Fig. 6C)**. Thus, these results illustrate the enhanced therapeutic efficacy of mitoDFX when used in combination with inhibitors of the glutathione antioxidant pathway.

We further focused on GPX4, a selenium-containing protein that protects cells from lipid peroxides using GSH as a substrate. GPX4 level was significantly induced by 50 nM mitoDFX exposure for 60 h in MCF7 and MDA-MB-231 cells, but not in BJ cells, suggesting a link between the accumulation of lipid peroxides and the induction of GPX4 **(Fig. 6D, E, and S8D)**. To further confirm that GPX4 induction is related to mitoDFX sensitivity, we knocked out or knocked down *GPX4* (KO and KD) in MCF7 cells **(Fig. S8E)** and observed enhanced cell death following treatment with 10 nM mitoDFX. As such treatment did not affect wild-type cells, this suggests an important role of GPX4 in coping with the toxic effect induced by mitoDFX **(Fig. 6F)**. Taken together, our results demonstrated that mitoDFX elevates ROS levels, which further causes the generation of lipid peroxides that are neutralized by GPX4 at the expense of GSH. However, mitoDFX eventually depletes and oxidizes GSH, rendering GPX4 unable to detoxify lipid peroxides, leading to the accumulation of toxic lipid peroxides and subsequent ferroptotic cell death.

MitoDFX inhibits tumor growth of syngeneic melanoma and TNBC cells as well as xenografted human TNBC in vivo.

Our *in vitro* results demonstrated a profound suppressive effect of mitoDFX on proliferation and its ability to induce cell death in breast cancer cell lines. Therefore, we assessed mitoDFX efficacy *in vivo*

using syngeneic and xenograft mouse models. In the syngeneic mouse models (4T1 and B16 cells), mitoDFX (intraperitoneal at 1 mg/kg or 0.25 mg/kg, respectively) significantly decreased tumor growth **(Fig. 7A)**. Similarly, in a breast cancer xenograft model (MDA-MB-231 cells), mitoDFX treatment (intraperitoneally at 1 mg/kg) markedly suppressed tumor progression **(Fig. 7B)**. Moreover, long-term oral treatment with mitoDFX markedly reduced tumor growth in a melanoma mouse model **(Fig. 7C)**. We also assessed complete hematological parameters (number of red blood cells (RBC), hemoglobin content (HGB), hematocrit (HCT), and number of white blood cells (WBC) in tumor-bearing mice and observed no difference between the control and mitoDFX-treated animals, except for a small decrease in the WBC count of treated Balb/c mice **(Fig. 7D)**. To confirm that mitoDFX targets cancer cells and does not affect systemic iron metabolism, we evaluated the liver, spleen, and tumor tissue iron levels in BALB/c, NOD scid gamma (NSG), and C57BL/6 mouse models. We did not observe any changes in these parameters in the treated animals, except for B16 tumor iron levels, which decreased in the mitoDFX-treated group, possibly due to the higher basal iron level in this type of tumor **(Fig. 7E)**. Finally, the body weight of mice treated with mitoDFX did not show significant changes, indicating that mitoDFX did not adversely affect animal well-being at the selected doses **(Fig. S9A)**.

Discussion

In the present study, we describe mitochondrially targeted deferasirox (mitoDFX), an iron chelator that selectively induces death in cancer cells at nanomolar concentrations. We tested this agent and compared it with the previously described mitoDFO (27) and its parental compound deferasirox (DFX). We observed a marked decrease in the IC_{50} value compared with that of both DFX and mitoDFO, with values in the range of 10-100 nM for selected cancer cells. This makes it approximately three orders of magnitude more effective than DFX and approximately 30 times more effective than mitoDFO,

14

suggesting that this chelator possesses some unique features that synergize with the effects of mitochondrial iron chelation.

Treatment with 50 nM mitoDFX induced iron deprivation, as evidenced by an increase in the protein level of transferrin receptor 1 and a decrease in the amount of ferritin, both of which are regulated by the cytosolic IRP/IRE system, suggesting that this system is activated despite targeting the chelator to the mitochondria. Furthermore, treatment with mitoDFX destabilizes iron-sulfur clusters and heme-containing proteins within the mitochondria, such as ETC components. However, our compound did not alter the cytosolic iron assembly machinery, indicating that alterations in iron utilization were limited to the mitochondria. Moreover, the low dose of mitoDFX (50 nM) specifically induced a reduction in mitochondrial iron level but did not affect total cellular iron, confirming the selective effect at low doses of mitoDFX. Importantly, these changes were not observed in non-malignant BJ fibroblasts under identical conditions, confirming the specificity of mitoDFX.

Based on our finding that mitoDFX significantly affects iron metabolism, we explored the possible molecular mechanisms responsible for its enhanced effect. We performed an unbiased proteomic analysis of the total cellular proteome using LC-MS, which confirmed the strong effect of mitoDFX on the mitochondrial proteome signature, with a dramatic decrease in the expression of many mitochondrial proteins. This analysis allowed us to further classify the groups of proteins that were deregulated and linked to certain cellular processes. As previously discussed, 50 nM mitoDFX significantly reduced some components of the ETC; however, there was also a strong effect on the components participating in mitochondrial transcription, translation, and DNA replication. Interestingly, the core components of mitochondrial transcription were significantly affected, including the mitochondrial RNA polymerase and RNA processing enzyme that cleaves polycistronic RNA into individual transcripts. These changes were in agreement with the observed marked decrease in the levels of all the mitochondrial transcripts. Furthermore, mitoDFX dramatically affected the components

needed for mitochondrial translation, and inhibition of this process was observed at multiple levels, the first being the amount of certain amino acid (AA) tRNA synthetases. This likely leads to a limited level of activated AAs being incorporated into the newly produced nascent proteins. Unexpectedly, one of the most deregulated groups of proteins were the components of the mitochondrial ribosomes that build both the 16S and 23S rRNA subunits. In many cases, the changes were so dramatic that the proteins could not be detected in the samples treated with mitoDFX, and the effect was strongest at a low dose of 50 nM for 60 h. This implies that mitochondrial translation was completely impaired after mitoDFX treatment. We hypothesized that this might be due to the recently revealed role of [Fe-S] clusters in the structure and function of mitochondrial ribosomes, which might represent a critical checkpoint specifically for mitochondrial translation(41, 42). Notably, we did not observe similar changes in the 40S and 60S subunits of eukaryotic ribosomes, which supports the unique role of [Fe-S] clusters in mitochondrial translation.

Treatment with mitoDFX also caused a metabolic rewiring, as evidenced by the significant reduction in citric acid, succinyl-CoA, fumarate, and malate and a dramatic drop in cis-aconitate, while there was a clear upregulation of pyruvate. This suggests that the TCA cycle is no longer running as a canonical cycle, and it appears that α-ketoglutarate has to be replenished by other metabolic reactions besides TCA because isocitrate levels are dramatically low; however, the level of α-ketoglutarate is stable. Furthermore, we detected a reduced level of fructose -1,6-bisphosphate and an increased NAD^+/NADH ratio. Since mitoDFX acts as an inhibitor of mitochondrial respiration, as indicated by the reduced oxygen consumption rate (OCR), one would expect to see an accumulation of NADH that is not being oxidized by the ETC. However, we observed a profound decrease in NADH levels, suggesting that it is either not produced by the TCA cycle or consumed by other processes, such as maintaining normal levels of reduced NADPH for antioxidant defense mechanisms. Indeed, when we inhibited the pentose phosphate pathway, one of the major sources of phosphate-reducing equivalents, we detected a clear

synergy with mitoDFX, supporting the notion that cells actively utilize this pathway to produce reducing equivalents to be used against oxidative insult (43).

The only mitochondrial protein that was significantly increased by mitoDFX treatment was glutathione peroxidase 4 (GPX4), a peroxidase that plays a key role in the regulation of ferroptosis (44) by eliminating toxic lipid peroxides using GSH as a reducing substrate. Oxidized GSSG is then reduced back to GSH by glutathione reductases using NADPH as the reducing equivalent. We observed a clear decrease in the GSH content, which was accompanied by an increase in lipid peroxidation after mitoDFX treatment. To further assess the role of GPX4 and glutathione metabolism in mitoDFX-induced cell death, we generated $GPX4^{-/-}$ KO and $GPX4^{-/+}$ KD MCF7 cell lines and observed a marked acceleration of cell death, confirming the involvement of this key ferroptosis regulator in the action of mitoDFX. Based on these findings, we believe that mitoDFX not only chelates mitochondrial iron and makes it biologically unavailable for iron-dependent cellular processes, but also exhausts the pool of the antioxidant agent glutathione. The combination of these two effects leads to the inability of GPX4 to prevent lipid peroxidation, culminating in oxidative cell death which resembles ferroptosis. This view is further supported by our observations that (i) blocking the synthesis of GSH by buthionine sulfoximine (BSO) or the import of cystine by sulfasalazine markedly synergizes with mitoDFX, (ii) cystine transporters SLC7A5 and SLC3A2 are induced by mitoDFX, and (iii) mitochondrial superoxide and mitochondrial lipid peroxides are produced in cancer cells exposed to mitoDFX. However, we should mention that we were unable to suppress mitoDFX-elicited death by either ferrostatin or liproxstatin (ferroptosis inhibitors), as shown in a report whose authors suggested that once oxidative damage exceeds a certain threshold, it can no longer be prevented by these compounds (45). An alternative explanation is that since iron ions are required for ferrostatin recycling (46), it is possible that mitoDFX actively prevents ferrostatin activity by scavenging iron ions.

Interestingly, cell death induced by mitoDFX shows similar characteristics to cell death elicited by ironomycin (47), including reduction of mitochondrial iron level, sensitivity to 6-AN, induction of phosphoglycerate dehydrogenase (PHGDH), reduction of OCR, and lack of response to caspase inhibitors and necrostatin. Yet, to stress the differences, we show that mitoDFX is even more potent compared to ironomycin as 50 nM mitoDFX completely blocks the proliferation of cells and induces cell death while ironomycin shows reduced proliferation only. Furthermore, mitoDFX is selective for cancer cells and its mode of action involves lipid peroxidation and glutathione depletion, which is indicative of ferroptosis and has not been observed with ironomycin.

In summary, mitochondrially targeted deferasirox (mitoDFX) has the unique ability to elicit iron deprivation and produce toxic lipid peroxides *via* its redox activity, thus harnessing the dual nature of iron in a single molecule to combat cancer. Importantly, the agent can effectively kill cancer cells at nanomolar concentrations while sparing non-malignant cells and has shown significant efficacy in animal models of triple-negative breast cancer and melanoma, allowing for oral administration of the drug. Therefore, mitoDFX represents a novel paradigm in the field of iron chelation, demonstrating that mitochondrial targeting of a redox-active iron chelator results in a highly effective agent against multiple types of cancer.

Methods

Cell line sources and culture conditions

Breast cancer cells (MCF7, MDA-MB-231 and T47D), melanoma cells (A375, B16, BLM, G361 and Malme-3M), lung cancer cells (A549, Calu-1, LLC1), pancreatic cancer cells (BxPC-3), ovarian cancer cells (OVCAR3) and non-malignant (BJ) cells were obtained from the American Type Culture Collection (ATCC). HFP-1 human fibroblasts were obtained from Dr. Smetana (Institute of Anatomy, Charles University, Prague, Czech Republic). All cells were cultured in a humid incubator at 37 °C with 5 % CO_2 in

DMEM (Sigma) supplemented with 10 % fetal bovine serum, 100 U/ml streptomycin/penicillin (Sigma), and 2 mM L-glutamine (PAN Biotech). Additionally, BxPC-3 cells were supplemented with non-essential amino acids (Sigma). Cultured cells were regularly tested for mycoplasma contamination and used within three months of defrosting.

mitoDFX synthesis

Dimethylformamide (DMF) (3 ml), was added to a round bottom flask containing Deferasirox[1,2] (114 mg, 0.31 mmol), 10-aminodecylphosphonium chloride hydrochloride (150 mg, 0.31 mmol), N-(3-dimethyl aminopropyl)-N⬚-ethylcarbodiimide hydrochloride (EDC) (88 mg, 0.46 mmol) and N, N-diisopropylethylamine (DIPEA) (0.32 ml, 1.86 mmol), and the reaction was stirred for 72 hours at room temperature. Solvents were evaporated and the mixture was dissolved in methanol (MeOH) and washed with citric acid (5 %, 7 mL), brine (7 mL), and dichloromethane (DCM, 2 × 20 mL). Column chromatography (2 % MeOH/CHCl$_3$) afforded the product (25 mg, 10 %) as a light-yellow foam **(Fig. S9B)**.

Cell viability assay

Viable cells were stained with crystal violet. Briefly, cells were seeded onto 96-well plates at a density of 1×10^4 cells/well and allowed to adhere overnight. The next day, the cells were treated with mitoDFX or DFX at the indicated concentrations for 48 h. After incubation, the cells were fixed with 4 % paraformaldehyde, washed with PBS, and stained with crystal violet overnight (0.05 % in water). The following day, the cells were washed with PBS, and crystals were solubilized in 1 % SDS. Absorbance was measured at 595 nm using a Tecan Infinity M200 microplate reader. IC$_{50}$ values were obtained by plotting the percentage of live cells versus the logarithm of the concentration of the compound.

Real-time cell proliferation and death monitoring

Live-cell imaging was performed using a Lumascope S720 (Etaluma). Briefly, 2×10^3 cells/well were seeded into 96-well plates and allowed to attach overnight. The next day, the cells were treated with either mitoDFX (0.03-1 µM), DFX (1-10 µM), BSO (100 µM), SSZ (500 µM), or 6-AN (10 µM). SYTOX green (0.5 µM, Thermo Scientific), an impermeable nucleic acid stain, was used to detect the dead cells. Bright-field and green fluorescence (SYTOX) images were captured for 72 h at 3 h intervals. Cell proliferation and death analyses were performed using Lumaview software and are presented as the percentage of confluence or the number of dead cells over time.

Flow cytometry

For all flow cytometry experiments, cells were seeded at a concentration of 1×10^5 per ml and allowed to attach overnight. The cells were then incubated with mitoDFX for the indicated times and stained with the corresponding probes. Finally, the cells were collected by trypsinization and analyzed using a BD LSRFortessa™ flow cytometer (BD Biosciences). Annexin V/propidium (AV/PI) double staining was measured at 489 nm_{Ex}/515 nm_{Em} for AV and 534 nm_{Ex}/617 nm_{Em} for PI. The percentage of dead cells is represented as the sum of AV+/PI–, AV–/PI+, and AV+/PI+ cells. Cell cycle was determined using Vybrant DyeCycle™ Violet Stain (Thermo Fisher Scientific) at 405 nm_{Ex}/437 nm_{Em}. Cellular ROS levels were measured using 2′,7′-dichlorofluorescein diacetate (DCF-DA; Sigma-Aldrich) at 488 nm_{Ex}/585 nm_{Em} while mitochondrial ROS levels were determined using the MitoSOX probe (ThermoFisher Scientific) at 488 nm_{Ex}/530nm_{Em}. Tetramethylrhodamine methyl ester (TMRM; Sigma-Aldrich) was measured at 561 nm_{Ex}/586 nm_{Em}. Lipid peroxidation in the mitochondrial membrane was determined using the MitoPeDPP fluorescent dye (Dojindo) and analyzed at 488 nm_{Ex}/530nm_{Em}.

Immunoblotting and antibodies information

20

For immunoblotting, cells were washed with PBS and lysed in radioimmunoprecipitation assay (RIPA) buffer supplemented with protease (SERVA) and phosphatase inhibitors (Roche). The protein concentration was determined using a Bicinchoninic Acid Protein (BCA) assay (Thermo Scientific) on a Tecan Infinity M200 microplate reader. Forty micrograms of protein were resolved by 10 % SDS-PAGE and transferred to PVDF membranes. Membranes were visualized using chemiluminescent substrates Western Bright Sirius (Advansta) or Clarity (BioRad) in an Azure c600 camera (Azure Biosystems). The antibodies used in this study are listed in Table S2.

Mitochondrial isolation, solubilization, and Blue-Native polyacrylamide (BN-PAGE) electrophoresis

To isolate mitochondria, cells were lysed by homogenization with a cell homogenizer (Isobiotech) in STE buffer (250 mM Sucrose, EDTA 1 mM, and 10 mM Tris), followed by differential centrifugation, as described in (27). The concentration of solubilized mitochondria in the supernatant was determined using the BCA method and used for blue native-PAGE electrophoresis.

The levels and organization of respiratory supercomplexes were analyzed in mitochondrial lysates using blue-native electrophoresis. Mitochondrial samples (25 µg) were loaded onto 3-12 % or 4-16 % gradient gels and run overnight at a constant 25 V. After electrophoresis, the gels were incubated with 0.1 % SDS in transfer buffer and visualized using the chemiluminescent substrate Western Bright Sirius in an Azure c600 camera. The antibodies used in this study are listed in Table S2.

Cellular ATP measurement

Total cellular ATP levels were measured using the CellTiter-Glo® Luminescent Cell Viability Assay kit (Promega), according to the manufacturer's instructions. $1x10^4$ cells were seeded in 96 well plates and incubated overnight for attachment. The next day, the cells were treated with mitoDFX (0.03- 1 µM) in the absence or presence of 2-DG (50 mM; Sigma) or oligomycin (2 µM; Sigma) for 4 h before

21

measurement. Graphs were generated by normalizing values to the total cell number measured by the

Alamar Blue™ HS Cell Viability Reagent (Thermo Scientific) and relative to the control condition.

Oxygen consumption rate measurement

The oxygen consumption rate (OCR) was measured using a seahorse XFe96 (Agilent Technologies), according to the manufacturer's protocol. $1x10^4$ cells/well were seeded in an XFe96 cell culture plate pretreated with poly-L-lysine (Sigma-Aldrich). The next day, cells were treated with increasing concentrations of mitoDFX (0.03, 0.1, and 1 µM) and incubated for 1 h. The XF96 sensor cartridge was loaded with oligomycin (1 µM; Port A), FCCCP (1 µM; Port B), Rotenone/Antimycin A (1 µM/1.8 µM; Port C), and Hoechst (2 µg/ml; Port D). Data were normalized to cell numbers obtained using the ImageXpress Micro XLS analysis system (Molecular Devices).

Confocal microscopy

Cellular and mitochondrial Fe^{2+} levels were assessed using FerroOrange (Dojindo) and MitoFerroGreen (Dojindo) probes, respectively, according to the manufacturer's instructions. Briefly, cells were seeded in a 35 mm dish with a glass insert (Cellvis) and incubated overnight for attachment. The next day, cells were incubated with mitoDFX for 24-60 h. Finally, cells were incubated with 1 µM FerroOrange, 5 µM MitoFerroGreen, 2 µM Hoechst 33342, or 20 nM MitoTracker Deep Red for 30 min at 37 °C, 5 % CO_2 in an incubator. The cells were observed under a Leica SP8 confocal microscope or a Nikon CSU-WI Spinning Disk confocal microscope, and images were acquired using a 63x water immersion objective detected at 543 nm_{Ex}/580 nm_{Em} for FerroOrange, 488 nm_{Ex}/535 nm_{Em} for MitoFerroGreen, 640 nm_{Ex}/663 nm_{Em} for MitoTracker and at 405 nm_{Ex}/450 nm_{Em} for Hoechst.

To detect mitophagy in cells, the fluorescent Mtphagy Detection Kit (Dojindo Laboratories, Japan) was used according to the manufacturer's instructions. Briefly, cells were seeded in a 35 mm dish with a glass insert and incubated overnight. The next day, the cells were washed twice with HBSS buffer and incubated with Mtphagy Dye (100 nM). After 30 min, the cells were washed twice with HBSS buffer, and a culture medium was added. The cells were then treated with mitoDFX (100 nM and 1 μM) for 24 h. On the day of imaging, the cells were incubated with the Lyso dye (1 μM; 30 min). Subsequently, cells were visualized using a 63x water immersion lens in a Leica SP8 confocal microscope at 561 nm_{Ex}/650 nm_{Em} for Mtphagy dye and 488 nm_{Ex}/510 nm_{Em}, for Lyso dye.

The mitochondrial network was evaluated in MCF7 cells transfected with mitochondrial GFP. Cells were seeded in a 35 mm dish with a glass insert and incubated overnight for attachment. After incubation, cells were treated with mitoDFX (1 μM for 24 h and 50 nM for 60 h). Afterward, cells were incubated in the presence of 2 μg/ml Hoechst 33342 and immediately imaged using a 63x water immersion lens in a Leica SP8 confocal microscope. Fluorescence was detected at 405 nm_{Ex}/450 nm_{Em} for Hoechst and 488 nm_{Ex}/510 nm_{Em} for GFP. Quantification of the fluorescence signal, radial analysis and object counting were performed using the ImageJ software, as described before (48).

Quantitative Polymerase chain reaction (qPCR) with reverse transcription

RNA isolation was performed using RNAzol RT (Molecular Research Centre), according to the manufacturer's instructions. The RNA quantity was measured using a NanoDrop spectrometer (Thermo Scientific, ND-1000). cDNA was generated using the RevertAid RT Reverse Transcription Kit (Fermentas), according to the manufacturer's instructions. Quantitative PCR (qPCR) was performed using a 5x HOT FIREpol Eva Green qPCR mix kit (Solis BioDyne) in 384-well plates. Triplicate samples were run on a c1000 Thermal cycler (BIORAD). The temperature profile set for the run was 95 °C for 12 min, followed by 40 cycles at 95 °C for 10 s, 60 °C for 25 s, and 72 °C for 20 s. Data were analyzed using GenEx software

version 6 and normalized to the reference gene RPLP0. The sequences and primers used for qPCR are listed in Table S3.

Determination of GSH and GSSG levels

The levels of reduced glutathione (GSH), total glutathione (GSH+GSSG), and the GSH/GSSG ratio were measured using the GSH/GSSG-Glo assay kit (Promega) according to the manufacturer's instructions. Cells were seeded in 96-well plates and allowed to attach overnight. The next day, cells were exposed to mitoDFX for 24 or 60 h at a concentration of 50 nM. After the given time, the cells were washed with PBS, and the total glutathione lysis reagent or oxidized glutathione lysis reagent was added to the designated wells. The cells were further incubated with the luciferin generation reagent for 30 min at RT. Finally, luciferin detection reagent was added to all wells, incubated for 15 min, and luminescence was measured. The amounts of total glutathione and oxidized glutathione were normalized to the cell number, which was measured using the Alamar Blue HS Cell Viability Reagent.

Determination of NAD+(P+)/ NAD(P)H levels

Cellular NAD^+/NADH and $NADP^+$/NADPH ratios were measured using the NAD/NADH-Glo Assay (Promega) and NADP/NADPH-Glo Assay kit (Promega), respectively, according to the manufacturer's instructions. Briefly, 1×10^4 cells/well were seeded in a 96-well plate and allowed to attach overnight. Cells were treated for 24-60 h with 50 nM mitoDFX, washed with PBS, and then specific assay reagents were used to detect each species. The amounts of NADH, NAD^+, NADPH, and $NADP^+$ were normalized to the cell number, which was measured using the Alamar Blue HS Cell Viability Reagent.

24

Proteomic nLC-MS 2 analysis

Samples were homogenized and lysed by boiling at 95 °C for 10 min in 100 mM TEAB (Triethylammonium bicarbonate) containing 2 % SDC (sodium deoxycholate), 40 mM chloroacetamide, and 10 mM Tris(2-carboxyethyl)phosphine, and further sonicated (Bandelin Sonoplus Mini 20, MS 1.5). Protein concentration was determined using the BCA protein assay kit (Thermo Fisher Scientific), and 30 μg of protein per sample was used for MS sample preparation. The samples were further processed using SP3 beads according to Hughes et al. (49).

All data were analyzed and quantified using MaxQuant software (version 1.6.12.0) (50, 51). The false discovery rate (FDR) was set to 1 % for both proteins and peptides, and a minimum peptide length of seven amino acids was specified. The Andromeda search engine was used to search MS/MS spectra against the human database (downloaded from UniProt.org, containing 20,598 entries). Data analysis was performed using the Perseus 1.6.15.0 software (52).

Metabolomic analysis

For metabolomic assays, cells were grown to confluence in a 100 mm petri dish, washed with ice-cold 0.9 % NaCl solution, and metabolites were extracted with 500 μL 80 % methanol + 2 μg/ml ribitol (internal standard). Protein quantification of the resulting pellets was performed for normalization.

Next, the samples were centrifuged, and the supernatants were evaporated and resuspended in 200 μL of 50 % acetonitrile containing internal standards (3.3 μM 1,4-piperazinediethanesulfonic acid, 1.5 μM $^{15}N_5$-AMP). The sample volume for injection was 1 μL. The samples were analyzed on a Dionex Ultimate 3000RS liquid chromatography system coupled to a TSQ Quantiva mass spectrometer (Thermo Scientific) using electrospray ionization in switching polarity mode with the following ion source parameters: ion transfer tube temperature 325 °C, vaporizer temperature 275 °C, spray voltage 3500/2800 V (positive/negative mode), sheath gas 35, and aux gas 7. A SeQuant® ZIC®-pHILIC column

25

(150 mm × 2.1 mm, 5 µm) coupled with a SeQuant® ZIC®-pHILIC Guard (20 mm × 2.1 mm) (Merck) was used for analyte separation. The buffer composition was A: 10 mM ammonium bicarbonate pH 9.3 and B: 97 % acetonitrile, at a flow rate of 200 µL/min. The elution gradient (A/B) used was 0 – 2.5 min: 5 % A; 2.5 – 21 min: 5 % A to 70 % A; followed by washing phase 21 – 23 min: 70 % A and equilibration phase 23.1 – 32 min: 5 % A. Selective reaction monitoring (SRM) was used for the detection and quantification of selected compounds. Data were processed using the Skyline software.

Mice experiments and ethical compliance

NOD scid gamma mice (NSG) and BALB/c mice were injected with $1x10^6$ MDA-MB-231 and 4T1 cells, respectively. C57BL/6 mice were injected with $2x10^5$ B16 cells. When the tumor volume reached 30-50 mm^3 (tumor size quantified using ultrasound imaging, USI), each group was further divided into two subgroups and treated intraperitoneally (i. p.) with either vehicle (2.5 % DMSO in corn oil, 100 µL per dose) or mitoDFX (1 mg/kg or 0.25 mg/kg in corn oil) twice per week. Moreover, another group of C57BL/6 mice was administered 1.5 µM mitoDFX orally (roughly equivalent to a 0.25 mg/kg dose) continuously through drinking water. The tumor volume was monitored using the USI instrument Vevo770 (VisualSonics). Once the tumor volume reached 1000 mm^3, mice were sacrificed and samples were obtained from the liver, spleen, blood, and tumor and used for the determination of several parameters.

Statistics

Statistical information for individual experiments can be found in the corresponding figure legends. All results are expressed as mean ± SEM of at least three independent experiments or 5 different animals. The comparison between treated samples and control was performed by one-way ANOVA or two-way ANOVA followed by Tukey's multiple comparison test or by Student's t-test, using GraphPad Prism

software version 10.1.1. The minimum significance level was set at $P < 0.05$. No statistical methods were used to determine the sample sizes.

Study approval

All mouse procedures were approved by the Czech Academy of Sciences and performed according to the Czech Republic Council guidelines for the Care and Use of Animals in Research and Teaching.

Data Availability

Raw proteomics data (**Fig. 4 and S3**) are provided as **Supplementary File 2**.

References

1.   Gallagher PS, et al. Iron homeostasis regulates facultative heterochromatin assembly in adaptive genome control. *Nat Struct Mol Biol.* 2018;25(5):372-83.
2.   Stehling O, et al. MMS19 assembles iron-sulfur proteins required for DNA metabolism and genomic integrity. *Science.* 2012;337(6091):195-9.
3.   Puig S, et al. The elemental role of iron in DNA synthesis and repair. *Metallomics.* 2017;9(11):1483-500.
4.   Lill R, and Freibert SA. Mechanisms of Mitochondrial Iron-Sulfur Protein Biogenesis. *Annu Rev Biochem.* 2020;89:471-99.
5.   Brown RAM, et al. Altered Iron Metabolism and Impact in Cancer Biology, Metastasis, and Immunology. *Front Oncol.* 2020;10:476.
6.   Sheftel AD, et al. The long history of iron in the Universe and in health and disease. *Biochim Biophys Acta.* 2012;1820(3):161-87.
7.   Andreini C, et al. The human iron-proteome. *Metallomics.* 2018;10(9):1223-31.
8.   Paul BT, et al. Mitochondria and Iron: current questions. *Expert Rev Hematol.* 2017;10(1):65-79.
9.   Pantopoulos K, et al. Mechanisms of mammalian iron homeostasis. *Biochemistry.* 2012;51(29):5705-24.
10.   Torti SV, and Torti FM. Iron and cancer: more ore to be mined. *Nat Rev Cancer.* 2013;13(5):342-55.
11.   Dixon SJ, et al. Ferroptosis: an iron-dependent form of nonapoptotic cell death. *Cell.* 2012;149(5):1060-72.
12.   Lui GY, et al. Targeting cancer by binding iron: Dissecting cellular signaling pathways. *Oncotarget.* 2015;6(22):18748-79.

13.   Merlot AM, et al. Novel chelators for cancer treatment: where are we now? *Antioxid Redox Signal.* 2013;18(8):973-1006.
14.   Rychtarcikova Z, et al. Tumor-initiating cells of breast and prostate origin show alterations in the expression of genes related to iron metabolism. *Oncotarget.* 2017;8(4):6376-98.
15.   Dizdaroglu M, and Jaruga P. Mechanisms of free radical-induced damage to DNA. *Free Radic Res.* 2012;46(4):382-419.
16.   Buss JL, et al. Iron chelators in cancer chemotherapy. *Curr Top Med Chem.* 2004;4(15):1623-35.
17.   Lui GY, et al. The iron chelator, deferasirox, as a novel strategy for cancer treatment: oral activity against human lung tumor xenografts and molecular mechanism of action. *Mol Pharmacol.* 2013;83(1):179-90.
18.   Amano S, et al. Invasion inhibition in pancreatic cancer using the oral iron chelating agent deferasirox. *BMC Cancer.* 2020;20(1):681.
19.   Krishan S, et al. The Anticancer Agent, Di-2-Pyridylketone 4,4-Dimethyl-3-Thiosemicarbazone (Dp44mT), Up-Regulates the AMPK-Dependent Energy Homeostasis Pathway in Cancer Cells. *Biochim Biophys Acta.* 2016;1863(12):2916-33.
20.   Bogdan AR, et al. Regulators of Iron Homeostasis: New Players in Metabolism, Cell Death, and Disease. *Trends Biochem Sci.* 2016;41(3):274-86.
21.   Kalinowski DS, and Richardson DR. The evolution of iron chelators for the treatment of iron overload disease and cancer. *Pharmacol Rev.* 2005;57(4):547-83.
22.   Keberle H. The Biochemistry of Desferrioxamine and Its Relation to Iron Metabolism. *Ann N Y Acad Sci.* 1964;119:758-68.
23.   Tury S, et al. The iron chelator deferasirox synergises with chemotherapy to treat triple-negative breast cancers. *J Pathol.* 2018;246(1):103-14.
24.   Harima H, et al. Deferasirox, a novel oral iron chelator, shows antiproliferative activity against pancreatic cancer in vitro and in vivo. *BMC Cancer.* 2016;16(1):702.
25.   Kim JL, et al. Iron chelator-induced apoptosis via the ER stress pathway in gastric cancer cells. *Tumour Biol.* 2016;37(7):9709-19.
26.   Ohyashiki JH, et al. The oral iron chelator deferasirox represses signaling through the mTOR in myeloid leukemia cells by enhancing expression of REDD1. *Cancer Sci.* 2009;100(5):970-7.
27.   Sandoval-Acuna C, et al. Targeting mitochondrial iron metabolism suppresses tumor growth and metastasis by inducing mitochondrial dysfunction and mitophagy. *Cancer Res.* 2021;81(9):2289-303.
28.   Murphy MP, and Smith RA. Targeting antioxidants to mitochondria by conjugation to lipophilic cations. *Annu Rev Pharmacol Toxicol.* 2007;47:629-56.
29.   Truksa J, et al. Mitochondrially targeted vitamin E succinate modulates expression of mitochondrial DNA transcripts and mitochondrial biogenesis. *Antioxid Redox Signal.* 2015;22(11):883-900.
30.   Rohlenova K, et al. Selective Disruption of Respiratory Supercomplexes as a New Strategy to Suppress Her2high Breast Cancer. *Antioxid Redox Signal.* 2017;26(2):84-103.
31.   Dong L, et al. Mitocans Revisited: Mitochondrial Targeting as Efficient Anti-Cancer Therapy. *Int J Mol Sci.* 2020;21(21).
32.   Begum HM, and Shen K. Intracellular and microenvironmental regulation of mitochondrial membrane potential in cancer cells. *WIREs Mech Dis.* 2023;15(3):e1595.
33.   Reelfs O, et al. A Powerful Mitochondria-Targeted Iron Chelator Affords High Photoprotection against Solar Ultraviolet A Radiation. *J Invest Dermatol.* 2016;136(8):1692-700.
34.   Cilibrizzi A, et al. The synthesis and properties of mitochondrial targeted iron chelators. *Biometals.* 2023;36(2):321-37.

35. Griss J, et al. ReactomeGSA - Efficient Multi-Omics Comparative Pathway Analysis. *Mol Cell Proteomics.* 2020;19(12):2115-25.
36. Scheibye-Knudsen M, et al. Protecting the mitochondrial powerhouse. *Trends Cell Biol.* 2015;25(3):158-70.
37. Gaschler MM, and Stockwell BR. Lipid peroxidation in cell death. *Biochem Biophys Res Commun.* 2017;482(3):419-25.
38. Shioji K, et al. Synthesis and properties of fluorescence probe for detection of peroxides in mitochondria. *Bioorg Med Chem Lett.* 2010;20(13):3911-5.
39. Patra KC, and Hay N. The pentose phosphate pathway and cancer. *Trends Biochem Sci.* 2014;39(8):347-54.
40. Xie Y, et al. Ferroptosis: process and function. *Cell Death Differ.* 2016;23(3):369-79.
41. Itoh Y, et al. Structure of the mitoribosomal small subunit with streptomycin reveals Fe-S clusters and physiological molecules. *Elife.* 2022;11.
42. Zhong H, et al. BOLA3 and NFU1 link mitoribosome iron-sulfur cluster assembly to multiple mitochondrial dysfunctions syndrome. *Nucleic Acids Res.* 2023.
43. TeSlaa T, et al. The pentose phosphate pathway in health and disease. *Nat Metab.* 2023;5(8):1275-89.
44. Ursini F, and Maiorino M. Lipid peroxidation and ferroptosis: The role of GSH and GPx4. *Free Radic Biol Med.* 2020;152:175-85.
45. Ingold I, et al. Selenium Utilization by GPX4 Is Required to Prevent Hydroperoxide-Induced Ferroptosis. *Cell.* 2018;172(3):409-22 e21.
46. Miotto G, et al. Insight into the mechanism of ferroptosis inhibition by ferrostatin-1. *Redox Biol.* 2020;28:101328.
47. Garciaz S, et al. Pharmacologic Reduction of Mitochondrial Iron Triggers a Noncanonical BAX/BAK-Dependent Cell Death. *Cancer Discov.* 2022;12(3):774-91.
48. Bravo-Sagua R, et al. mTORC1 inhibitor rapamycin and ER stressor tunicamycin induce differential patterns of ER-mitochondria coupling. *Sci Rep.* 2016;6:36394.
49. Hughes CS, et al. Single-pot, solid-phase-enhanced sample preparation for proteomics experiments. *Nat Protoc.* 2019;14(1):68-85.
50. Cox J, and Mann M. MaxQuant enables high peptide identification rates, individualized p.p.b.-range mass accuracies and proteome-wide protein quantification. *Nat Biotechnol.* 2008;26(12):1367-72.
51. Cox J, et al. Accurate proteome-wide label-free quantification by delayed normalization and maximal peptide ratio extraction, termed MaxLFQ. *Mol Cell Proteomics.* 2014;13(9):2513-26.
52. Tyanova S, et al. The Perseus computational platform for comprehensive analysis of (prote)omics data. *Nat Methods.* 2016;13(9):731-40.

Acknowledgments

Author contributions

S.B. J: performed most of the *in vitro* experiments and helped with all *in vivo* experiments, analyzed and interpreted the data, curated the figures, and wrote, reviewed, and edited the manuscript. **C.S.A**: helped with *in vitro* experiments and led the *in vivo* experiments, analyzed and interpreted the data, supervised and designed experiments, generated the figures, and wrote, reviewed, and edited the manuscript. **Y.P.:** performed some of the *in vitro* experiments and helped *in vivo* experiments. **R.S.:** provided NSG mice and funding. **K.K, K.B, J.S, L.W:** synthesized the mitoDFX and helped with the experimental design. **J.T:** Conceptualized and obtained funding for the project, supervised the study, established collaborations, helped in designing experiments, analyzed and interpreted the data, and wrote, reviewed, and edited the manuscript.
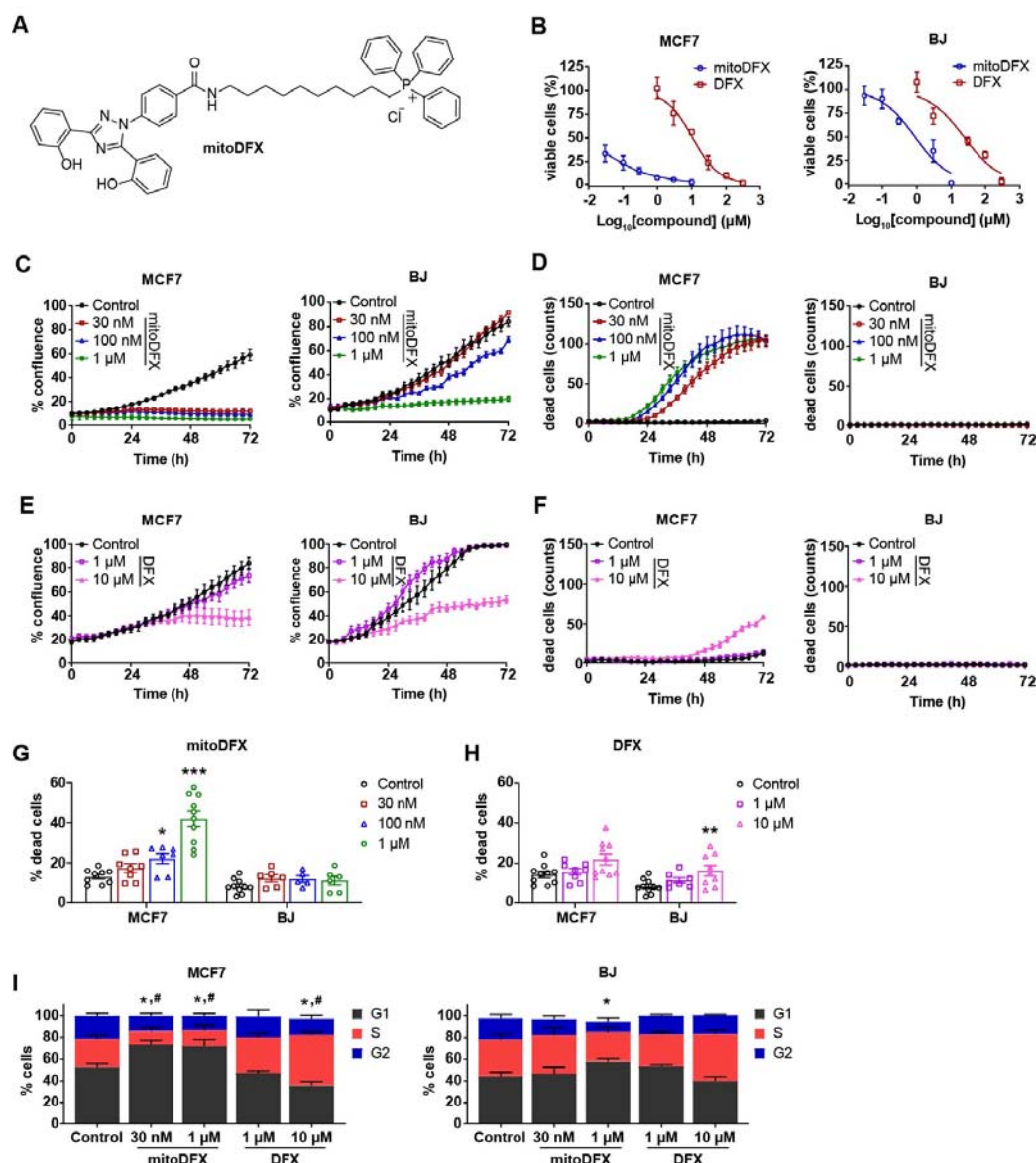
Figures

Figure 1

Figure 1: mitoDFX treatment induces cytostatic and cytotoxic effects in breast cancer cells. (A) Structure of mitoDFX. **(B)** Viability of MCF7 breast cancer cells and BJ human fibroblasts treated with mitoDFX and DFX for 48 h. Real-time monitoring of **(C)** proliferation and **(D)** cell death of MCF7 and BJ cells treated with mitoDFX. Cell death was measured using Sytox green dye (0.5 μM) and dead cells were counted in one field per well. Proliferation **(E)** and cell death **(F)** of MCF7 and BJ cells treated with DFX for 72 h using real-time LumaScope 720 microscope. Cell death was measured using Sytox green dye (0.5 μM). Percentage of dead MCF7 and BJ cells treated with **(G)** mitoDFX and **(H)** DFX, stained with annexin V and propidium iodide after 48 h. **(I)** Cell cycle distribution was assessed in MCF7 and BJ cells treated with indicated concentrations of mitoDFX and DFX and analyzed by FlowJo software. All data represents mean ± SEM of three independent experiments with at least two replicates each. P values were calculated by one-way **(G-H)** or two-way **(I)** ANOVA followed by Tukey's multiple comparisons test. **$P < 0.01$, ***$P < 0.001$ relative to Control and * $P ⬚ 0.05$ relative to the G_1 phase in the control; # $P ⬚ 0.05$ relative to the S phase in the control **(I)**.
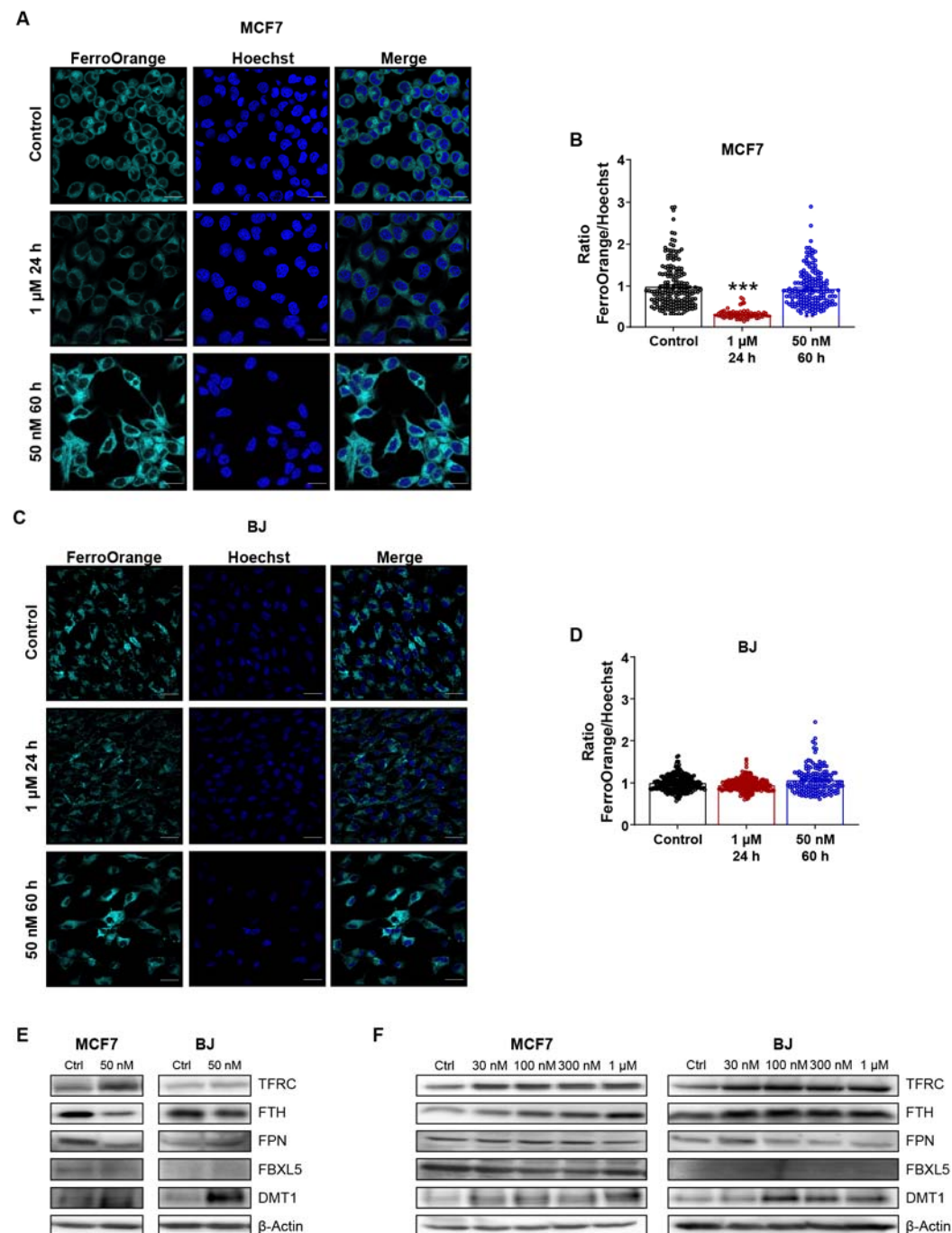
Figure 2

Figure 2: mitoDFX disrupts iron metabolism. (A, B) Confocal images of MCF7 and BJ cells treated with mitoDFX for short (24 h) and long term (60 h) and incubated with FerroOrange (1 µM) for 30 mins. Nuclei were stained with Hoechst 33342. **(C, D)** Quantification of the ratio of FerroOrange/Hoechst fluorescence relative to the control in MCF7 and BJ cells. **(E-F)** Western blot images of proteins related to iron metabolism in MCF7 and BJ cells treated with mitoDFX for short (24 h) and long term (60 h). All data represent mean ± SEM of three independent experiments with at least 50 cells each. P values were calculated by one-way ANOVA followed by Tukey's multiple comparisons test **(B, D)**. ***$P < 0.001$ relative to Control. Scale bars = 20 µm **(A, C)**.
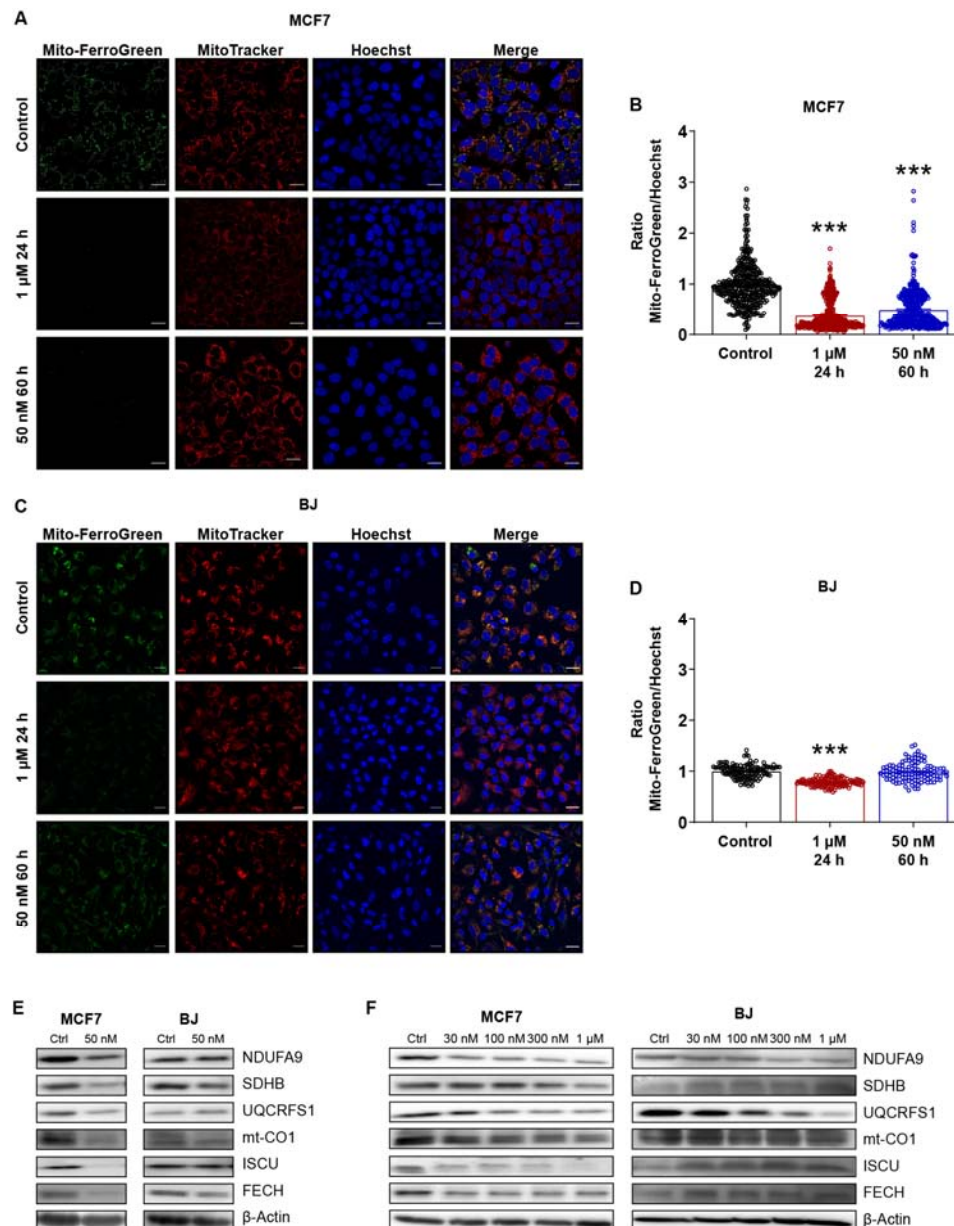
33

Figure 3

Figure 3: mitoDFX reduces mitochondrial biogenesis of [Fe-S] cluster and heme. (A, C) Confocal images of MCF7 and BJ cells treated with mitoDFX for short (24 h) and long term (60 h) and incubated with Mito-FerroGreen (5 μM). Nuclei were stained with Hoechst 33342. **(B, D)** Quantification of the ratio of Mito-FerroGreen/Hoechst fluorescence relative to control in MCF7 and BJ cells. **(E-F)** Western blot images of mitochondrial [Fe-S] cluster and heme-containing proteins metabolism in MCF7 and BJ cells treated with mitoDFX for long term (60 h). All data represent mean ± SEM of three independent experiments with at least 50 cells each. P values were calculated by one-way ANOVA followed by Tukey's multiple comparisons test **(B, D)**. ***$P < 0.001$ relative to Control. Scale bars = 20 μm **(A, C)**.
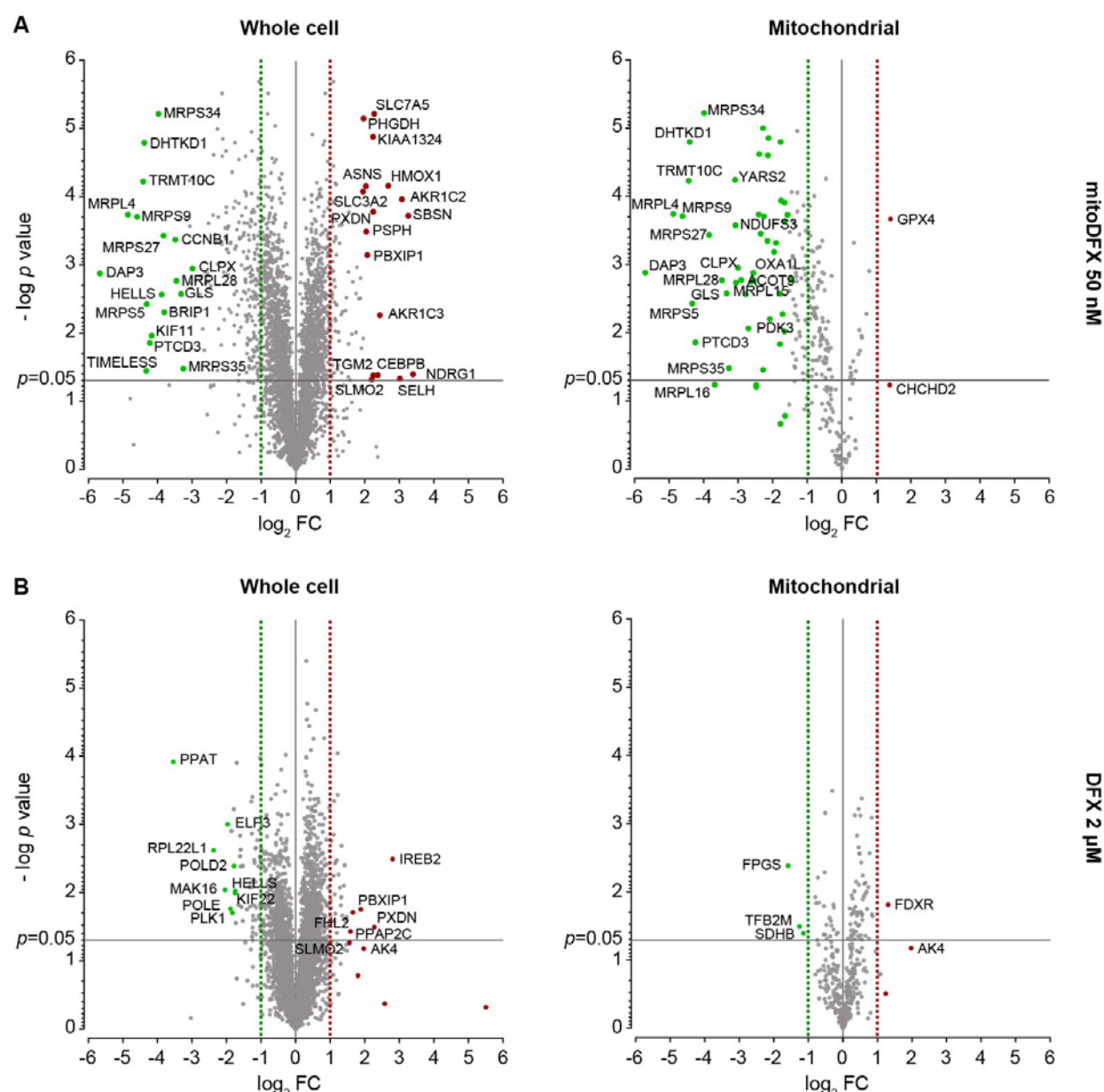
Figure 4

Figure 4: Proteomic profiling in malignant MCF7 cells under mitoDFX or DFX treatment. Volcano plots showing proteins detected by LC-MS in whole cell lysate and mitochondrial samples treated with **(A)** mitoDFX 50 nM or **(B)** DFX 2 μM for 60 h. The red points represent proteins that were upregulated with the treatments (p-value < 0.05, |fold change| > 2). The green points represent proteins that were downregulated with the treatments (p-value < 0.05, |fold change| > 2). Data was obtained from three independent experiments.
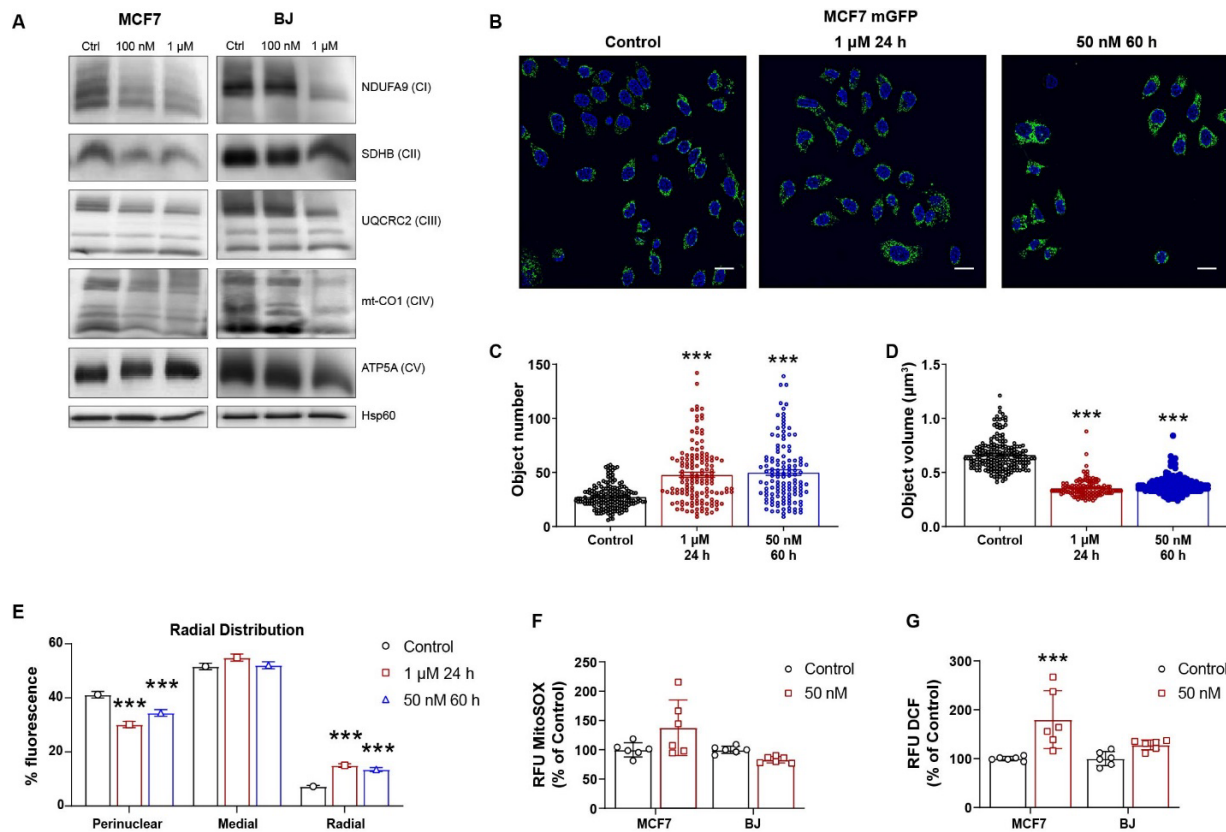
Figure 5

Figure 5: mitoDFX inhibits mitochondrial respiration, disrupts mitochondrial function and induces oxidative stress. (A) BN-PAGE of the OXPHOS complexes from isolated mitochondrial samples obtained from MCF7 and BJ cells treated with mitoDFX for 24 h. Hsp60 was used as a loading control. **(B)** Confocal images of MCF7-mitoGFP cells subjected to treatment with mitoDFX for 24-60 h. Nuclei were stained with Hoechst 33342. Scale bars = 20 μm. Quantification of mitochondrial number **(C)** and average volume **(D)** in MCF7-mitoGFP transfected cells treated with mitoDFX for 24-60 h. **(E)** Quantification of mitochondrial distribution in MCF7-mitoGFP cells exposed to mitoDFX for 24-60 h. Quantification of **(F)** mitochondrial and **(G)** cellular ROS levels after treatment with mitoDFX for 60 h in MCF7 and BJ cells respectively. All data represent mean ± SEM of three independent experiments with at least two replicates each. P values were calculated by one-way **(C-D) or** two-way ANOVA **(E)** ANOVA followed by Tukey's multiple comparison, two-tailed unpaired t-test **(F-G)**. **$*P < 0.01$, ***$P < 0.001$ relative to Control.
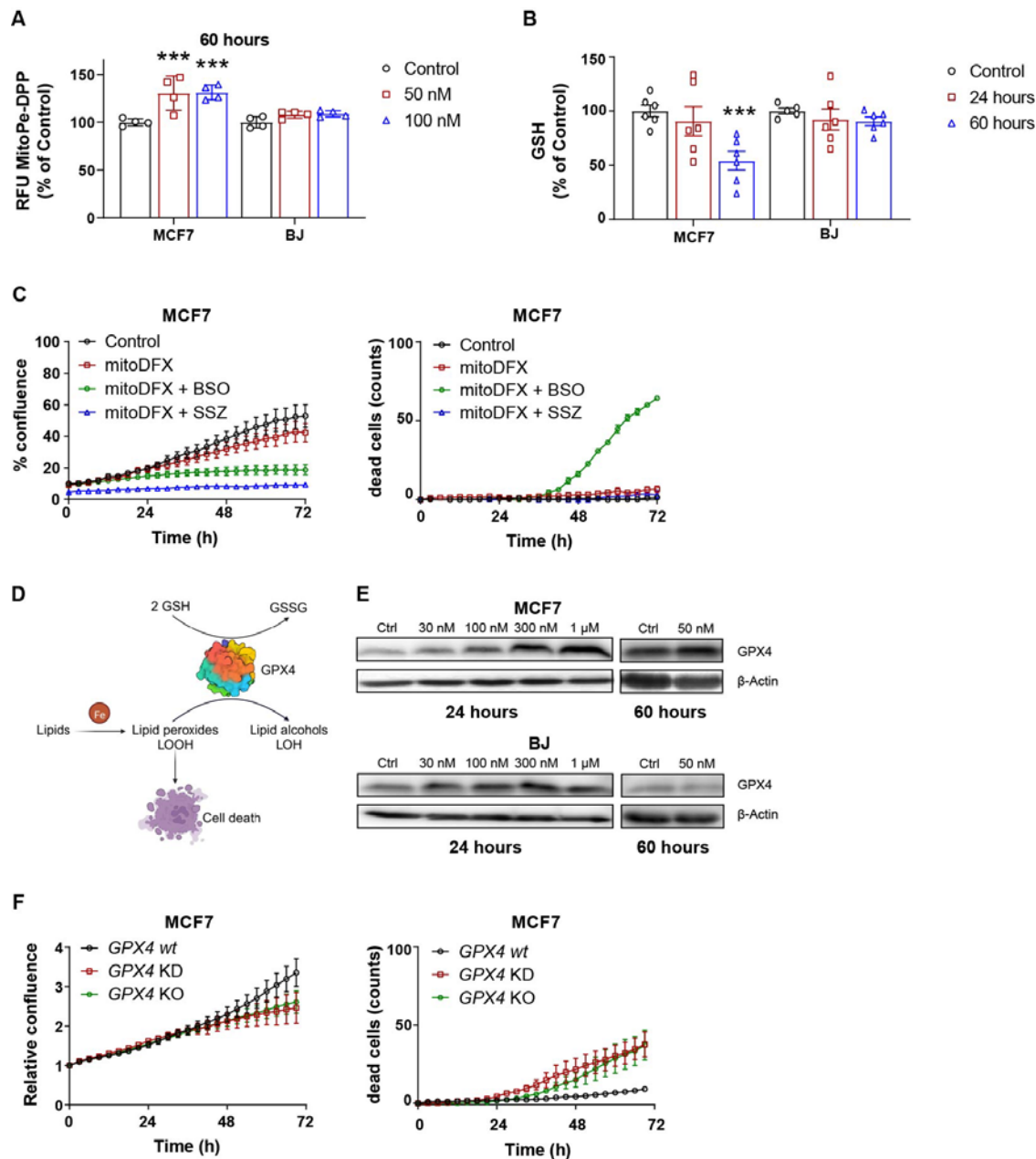
Figure 6

Figure 6: mitoDFX induces lipid peroxidation, and upregulates glutathione antioxidant defense mechanism. **(A)** Quantification of lipid peroxidation after mitoDFX treatment for 60 h in MCF7 and BJ cells. **(B)** Quantification of reduced glutathione (GSH) levels in MCF7 and BJ cells incubated with mitoDFX (50 nM) for short and long term. **(C)** Real-time monitoring of proliferation and cell death of MCF7 cells treated with mitoDFX (10 nM) in combination with buthionine sulfoximine (BSO; 100 μM) or sulfasalazine (SSZ; 500 μM) for 72 h. Cell death was measured using Sytox green dye (0.5 μM). **(D)** Schematic representation of the role of GPX4 in lipid peroxide detoxification. **(E)** Western blot images of GPX4 protein levels in MCF7 and BJ cells treated with mitoDFX for 24-60 h. **(F)** Real-time monitoring of proliferation and cell death of MCF7 (10 nM) *GPX4* KD and KO cells incubated with mitoDFX for 72 h. Cell death was measured using Sytox green dye (0.5 μM). All data represent mean ± SEM of three independent experiments with at least two replicates each. *P* values were calculated by two-way ANOVA **(A-B)** followed by Tukey's multiple comparison. **$P < 0.01$, ***$P < 0.001$ relative to Control.
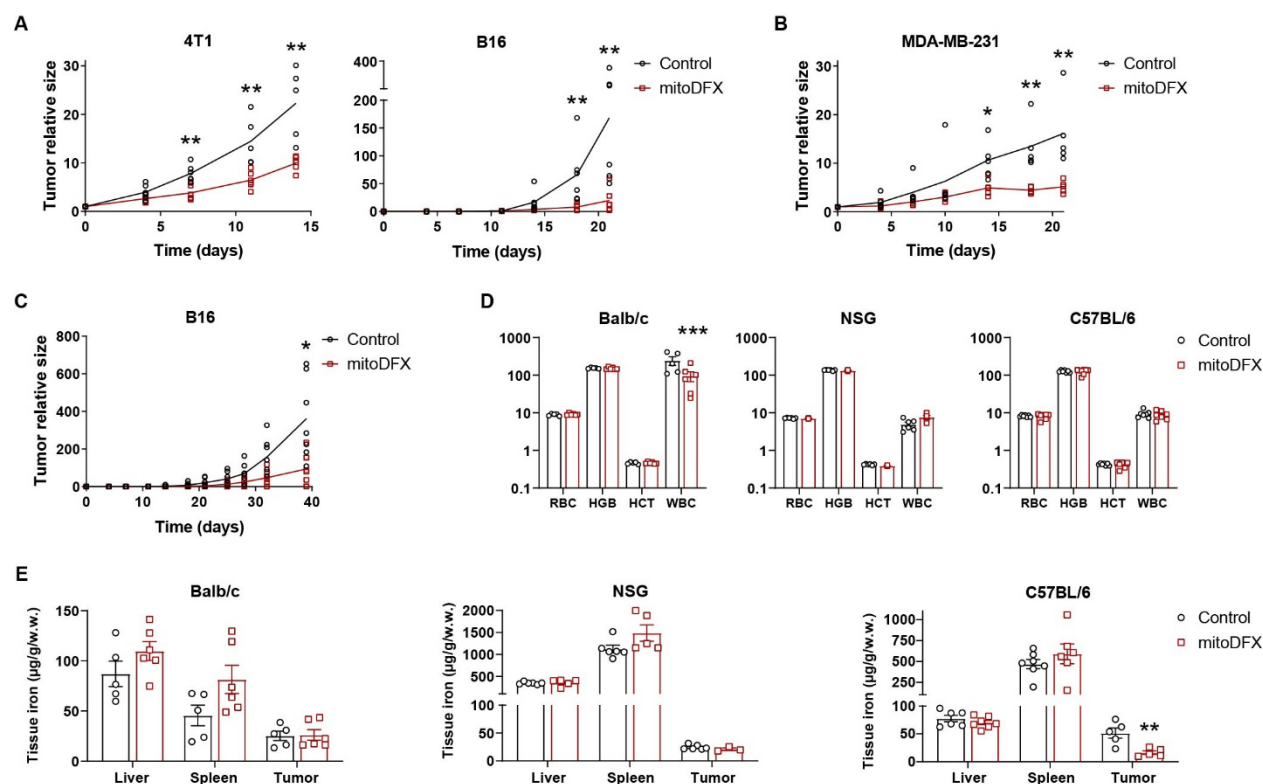
Figure 7

Figure 7: Antitumor effects of mitoDFX in mice models. Tumor growth curves of mice injected subcutaneously with **(A)** 4T1 and B16 and **(B)** MDA-MB-231 cells and treated with mitoDFX every 2 days for 14-21 days. When the tumor volume reached approximately 5-30 mm^3, the mice received mitoDFX i.p. (1 mg/kg for 4T1 and MDA-MB-231, and 0.25 mg/kg for B16). **(C)** Tumor growth charts of mice injected subcutaneously with B16 cells and continuously given mitoDFX in drinking water (1.5 μM) for 40 days. **(D)** Quantification of total red blood cells (RBC), hematocrit (HCT), hemoglobin (HGB), and white blood cells (WBC) in BALB/c, NSG, and C57BL/6 tumor-bearing mice treated i.p. with mitoDFX twice per week as mentioned above. **(E)** The iron content of liver, spleen, and tumor in BALB/c, NSG, and C57BL/6 tumor-bearing mice treated i.p. with mitoDFX twice per week as mentioned above. All data represent the mean ± SEM of at least 5 animals. P values were calculated by a two-tailed unpaired t-test. * $P \leq 0.05$, ** $P \leq 0.01$, *** $P \leq 0.001$ relative to Control.